# Multi-centre, multi-vendor reproducibility of 7T QSM and $R_2$* in the human brain: results from the UK7T study

Catarina Rua[a*], William T Clarke[b], Ian D Driver[c], Olivier Mougin[d], Andrew T. Morgan[e], Stuart Clare[b], Susan Francis[d], Keith Muir[e], David Porter[e], Richard Wise[c], Adrian Carpenter[a], Guy Williams[a], James B Rowe[f,g], Richard Bowtell[d], Christopher T Rodgers[a]

a) Wolfson Brain Imaging Centre, Department of Clinical Neurosciences, University of Cambridge, Cambridge, United Kingdom.
(The Wolfson Brain Imaging Centre, Box 65, Cambridge Biomedical Campus, Cambridge, UK, CB2 0QQ)

b) Wellcome Centre for Integrative Neuroimaging, FMRIB, Nuffield Department of Clinical Neurosciences, University of Oxford, Oxford, United Kingdom.
(Wellcome Centre for Integrative Neuroimaging, FMRIB, Level 0, John Radcliffe Hospital, Oxford, United Kingdom, OX3 9DU)

c) Cardiff University Brain Research Imaging Centre, School of Psychology, Cardiff University, Cardiff, United Kingdom.
(Cardiff University Brain Research Imaging Centre, Cardiff University, Maindy Road, Cardiff, CF24 4HQ)

d) Sir Peter Mansfield Imaging Centre, School of Physics and Astronomy, University of Nottingham, Nottingham, United Kingdom.
(Sir Peter Mansfield Imaging Centre, University of Nottingham, University Park, Nottingham, NG7 2RD)

e) Imaging Centre of Excellence, University of Glasgow, Glasgow, United Kingdom
(Imaging Centre of Excellence, Queen Elizabeth University Hospital, Langlands Dr, Glasgow, United Kingdom, G51 4LB)

f) Department of Clinical Neurosciences and Cambridge University Hospitals NHS Trust, University of Cambridge, Cambridge, United Kingdom
(Department of Clinical Neurosciences, Herchel Smith Building, Cambridge Biomedical Campus, Cambridge CB2 0SZ)

g) Medical Research Council Cognition and Brain Sciences Unit, University of Cambridge, Cambridge, United Kingdom.
(MRC Cognition and Brain Sciences Unit, University of Cambridge, 15 Chaucer Road, Cambridge, CB27EF)

* To whom correspondence should be addressed

## Abstract

We present the reliability of ultra-high field $T_2$* MRI at 7T, as part of the UK7T Network's "Travelling Heads" study. $T_2$*-weighted MRI images can be processed to produce quantitative susceptibility maps (QSM) and $R_2$* maps. These reflect iron and myelin concentrations, which are altered in many pathophysiological processes. The relaxation parameters of human brain tissue are such that $R_2$* mapping and QSM show particularly strong gains in contrast-to-noise ratio at ultra-high field (7T) *vs* clinical field strengths (1.5 - 3T). We aimed to determine the inter-subject and inter-site reproducibility of QSM and $R_2$* mapping at 7T, in readiness for future multi-site clinical studies.

Methods: Ten healthy volunteers were scanned with harmonised single- and multi-echo $T_2$*-weighted gradient echo pulse sequences. Participants were scanned five times at each "home" site and once at each of four other sites. The five sites had 1x Philips, 2x Siemens Magnetom, and 2x Siemens Terra scanners. QSM and $R_2$* maps were computed with the Multi-Scale Dipole Inversion (MSDI) algorithm (https://github.com/fil-physics/Publication-Code). Results were assessed in relevant subcortical and cortical regions of interest (ROIs) defined manually or by the MNI152 standard space.

Results and Discussion: Mean susceptibility ($\chi$) and $R_2$* values agreed broadly with literature values in all ROIs. The inter-site within-subject standard deviation was 0.001 – 0.005 ppm ($\chi$) and 0.0005 – 0.001 $ms^{-1}$ ($R_2$*). For $\chi$ this is 21-95% better than 3T reports, and 15-124% better for $R_2$*. The median ICC from within- and cross-site $R_2$* data was 0.98 and 0.91, respectively. Multi-echo QSM had greater variability *vs* single-echo QSM especially in areas with large $B_0$ inhomogeneity such as the inferior frontal cortex. Across sites, $R_2$* values were more consistent than QSM in subcortical structures due to differences in $B_0$-shimming. On a between-subject level, our measured $\chi$ and $R_2$* cross-site variance is comparable to within-site variance in the literature, suggesting that it is reasonable to pool data across sites using our harmonised protocol.

Conclusion: The harmonized UK7T protocol and pipeline delivers over a 2-fold improvement in the coefficient of reproducibility for QSM and $R_2$* at 7T compared to previous reports of multi-site reproducibility at 3T. These protocols are ready for use in multi-site clinical studies at 7T.

## Keywords

7 tesla; MRI; Quantitative Susceptibility Mapping; $R_2$* mapping; Multi-centre; Reproducibility.

## 1. Introduction

Neurodegenerative diseases are a significant global health burden. In many instances, neurodegeneration is associated with the deposition of iron in the brain. Understanding the patterns of deposition and their association with other risk factors is a key area of clinical research, but progress has been limited by the need to scale over multi-centre trials.

A popular approach to estimating iron concentration in the human brain uses gradient-echo (GE) magnetic resonance imaging (MRI). In grey matter, iron is mainly found in the protein ferritin, where it exists in a paramagnetic state (Langkammer et al., 2012). This paramagnetic iron interacts with the MRI scanner's static magnetic field ($B_0$) causing local dipolar field perturbations. These accentuate the rate of transverse signal decay causing $T_2$* relaxation in surrounding tissue, which is visible as decreasing signal amplitude with increasing echo time in a series of GE images. This effect causes an increase in the *rate* of transverse relaxation, $R_2$*, which correlates well with non-heme iron concentrations in grey matter (Gelman et al., 1999; Langkammer et al., 2010), and has been used to investigate the distribution of iron in the healthy brain and in disease (Haacke et al., 2005; Yao et al., 2009; Li et al., 2019).

The local presence of iron (and to a lesser extent myelin and calcium) also affects the signal phase of GE images because of the effect of the field perturbation on the local Larmor frequency (House et al., 2007; He et al., 2009; Lee et al., 2012). Quantitative Susceptibility Mapping (QSM) methods attempt to deconvolve these dipole phase patterns to identify the sources of the magnetic field inhomogeneity. In other words, QSM estimates quantitative maps of tissue magnetic susceptibility $\chi$ from GE phase data (Li and Leigh, 2004; Reichenbach, 2012; Wang and Liu, 2015). This approach has shown sensitivity to several neurological conditions (Lotfipour et al., 2012; Acosta-Cabronero et al., 2013; Blazejewska et al., 2015; Acosta-Cabronero et al., 2016) and offers advantages over magnitude $R_2$* such as having reduced blooming artifacts or being able to distinguish between paramagnetic and diamagnetic substances (Eskreis-Winkler et al., 2017).

$R_2$* imaging and QSM have been shown to provide reproducible results in single-site and cross-site studies at 1.5T and 3T (Hinoda et al., 2015; Cobzas et al., 2015; Deh et al., 2015; Lin et al., 2015; Santin et al., 2017; Feng et al., 2018; Spincemaille et al., 2019).

The dipole-inversion problem at the heart of QSM methods benefits from the increased sensitivity to magnetic susceptibility variation and spatial resolution at ultra-high fields ($B_0 \geq 7$ T) (Yacoub et al., 2001; Reichenbach et al., 2001; Tie-Qiang et al., 2006; Duyn et al., 2007; Wharton and Bowtel, 2010). At 7T, close attention must be paid to $B_0$ shimming and gradient linearity to achieve accurate QSM and $R_2$* mapping (Yang et al., 2010). Head position is also an important factor that affects the susceptibility anisotropy (Lancione et al., 2017; Li et al., 2017).

In this study, we introduce single-echo and multi-echo GE imaging protocols for QSM and $R_2$* mapping at 7T which were standardised on three different 7T MRI scanner platforms, from two different vendors. We applied this standardised protocol in the UK7T Network's "Travelling Heads" study on 10 subjects scanned at 5 sites. We report reproducibility for derived $R_2$* and QSM maps and make recommendations for the design of future multi-centre studies.

| # Site | | Vendor | Scanner Model | Gradient Performance | Installation Date (Month-Year) | Software Version |
|---|---|---|---|---|---|---|
| 1 | Wellcome Centre for Integrative Neuroimaging (FMRIB), University of Oxford | Siemens | Magnetom 7T | 70 mT $m^{-1}$<br>200 mT $m^{-1}$ $ms^{-1}$ | Dec-2011 | VB17A |
| 2 | Cardiff University Brain Research Imaging Centre, Cardiff University | Siemens | Magnetom 7T | 70 mT $m^{-1}$<br>200 mT $m^{-1}$ $ms^{-1}$ | Dec-2015 | VB17A |
| 3 | Sir Peter Mansfield Imaging Centre, University of Nottingham | Philips | Achieva 7T | 40 mT $m^{-1}$<br>200 mT $m^{-1}$ $ms^{-1}$ | Sep-2005 | R5.1.7.0 |
| 4 | Wolfson Brain Imaging Centre, University of Cambridge | Siemens | Magnetom Terra | 80 mT $m^{-1}$<br>200 mT $m^{-1}$ $ms^{-1}$ | Dec-2016 | VE11U |
| 5 | Imaging Centre of Excellence, University of Glasgow | Siemens | Magnetom Terra | 80 mT $m^{-1}$<br>200 mT $m^{-1}$ $ms^{-1}$ | Mar-2017 | VE11U |

**Table 1:** Details of the scanners and hardware used for the UK7T Network's Travelling Heads study.

# 2. Methods

## 2.1. Measurement setup

Ten healthy volunteers (3 female, 7 male; age 32.0±5.9 years) were recruited: comprising two subjects from each of the five 7T imaging sites in the UK7T Network (described in Table 1). Each subject was scanned five times at their "home" site, and once at the other sites, under local ethics approval for multi-site studies obtained at Site-4 (HBREC.2017.08). Scans for each subject were completed within a period of between 83 and 258 days.

In every scan session, $B_0$ shimming was performed using the vendors' default second-order (or third-order for Site-4 and Site-5) $B_0$-shimming routines. $B_1^+$-calibration was performed initially using the vendor's default adjustment scans. A 3D DREAM sequence (Nehrke et al., 2012; Ehses et al., 2019) was subsequently acquired and the transmit voltage (or power attenuation) was then adjusted for all subsequent imaging based on the mean flip-angle from the brain in an anatomically-specified axial slice of the 3D DREAM flip angle map as described in Clarke et al. (2019). Single-echo (SE) 0.7mm isotropic resolution $T_2$*-weighted GE data were then acquired with: TE/TR=20/31ms; FA=15°; bandwidth=70Hz/px; in-plane acceleration-factor=4 (Sites-1/2/4/5) or 2x2 (Site-3); FOV=224x224x157mm$^3$; scan-time=~9min. Multi-echo (ME) 1.4mm isotropic resolution $T_2$*-weighted GE data were acquired with: $TE_1$/TR=4/43ms; 8 echoes with monopolar gradient readouts; echo-spacing=5ms; FA=15°; bandwidth=260Hz/px; acceleration-factor=4 (Sites-1/2/4/5) or 2x1.5 (Site-3); FOV=269x218x157mm$^3$; scan-time ~6min (Sites-1/2/4/5) and ~4min (Site-3). For Siemens data, coil combination was performed using a custom implementation of Roemer's algorithm, as previously described (Clarke et al., 2019). Subject 6's SE scan failed to reconstruct using Roemer's method on data from the 1$^{st}$ visit at Site-5 so a sum-of-squares (SoS) algorithm was used for coil combination for that scan instead. A 0.7mm isotropic MP2RAGE scan was used for within- and cross-site registration as previously described (Mougin et al., 2019).

### 2.2. QSM and $R_2$* data processing

QSM maps were generated from both the SE and ME $T_2$*-weighted datasets using the Multi-Scale Dipole Inversion (MSDI) algorithm, as implemented in QSMbox v2.0 (Acosta-Cabronero et al., 2018). Briefly: first the local field was estimated by phase unwrapping (Abdul-Rahman et al., 2005) and weighted least squares phase echo fitting was performed on the ME data. Then, for both SE and ME data, background field was removed using the Laplacian Boundary Value (LBV) method followed by the variable Spherical Mean Value (vSMV) algorithm with an initial kernel radius of 40mm (Zhou et al., 2014; Acosta-Cabronero et al., 2018). MSDI inversion was estimated with two scales: the self-optimised lambda method was used on the first scale with filtering performed using a kernel with 1mm radius, and on the second scale the regularization term was set to $\lambda=10^{2.7}$ (the optimal value for *in-vivo* 7T datasets found in (Acosta-Cabronero et al., 2018)) and filtering was done with a kernel radius set to 5mm. Brain masks used in the analysis were obtained with FSL's Brain Extraction Tool (BET) with fractional intensity threshold=0.2 for SE data (Smith, 2002). These were then mapped to ME data space.

On the ME data, QSM was reconstructed seven more times: with the shortest echo (TE1=4 ms), with the two shortest echoes (i.e. $TE_1/TE_2$ = 4/9 ms), with the three shortest echoes (i.e. $TE_1/TE_2/TE_3$ = 4/9/14 ms), and so forth.

On the ME dataset, voxel-wise quantitative maps of $R_2$* were obtained using the Auto-Regression on Linear Operations (ARLO) algorithm for fast monoexponential fitting (Pei et al., 2015).

### 2.3. Data Registration

The neck was cropped from the magnitude data with FSL's "robustfov" command (https://fsl.fmrib.ox.ac.uk/fsl/), applied to the SE data and the 4$^{th}$ echo of the ME data. High-resolution SE and ME templates were made from this cropped data for each subject with antsMultivariateTemplateConstruction2.sh from the Advanced Normalization Tools (ANTs, http://stnava.github.io/ANTs/). Two approaches were compared: transformations using rigid registration with mutual information similarity metric (denoted as "Rigid" below) or using symmetric diffeomorphic image registration

with cross-correlation similarity metric (denoted "SyN" below). Other settings were kept the same for both approaches: 4 steps with 0.1 gradient step size, maximum iterations per step 1000, 500, 250 and 100, smoothing factors per step of 4, 3, 2, and 1 voxels, and shrink factors per step of 12x, 8x, 4x, and 2x. The resulting registrations were then applied to the QSM and $R_2$* maps which were averaged to create SE and ME QSM and $R_2$* templates for each subject.

### 2.4. Selection of Regions of Interest (ROIs)

Five regions of interest (Substantia Nigra, Red Nucleus, Caudate Nucleus, Putamen and Globus Pallidus) were manually segmented based on the subject-specific QSM templates of the SE data registered with the "SyN" approach. In order to minimize the amount of segmentation variability, these ROIs were then mapped to the SE "Rigid", and ME "SyN" and ME "Rigid" spaces with nearest neighbour interpolation and via non-linear registrations obtained with the default settings in the antsRegistrationSyN.sh command in ANTs.

Magnitude data were first registered to the $T_1$-weighted MP2RAGE scans (Rigid transformations; MI similarity metric) and later to the standard $T_1$ "MNI152 brain" (Montreal Neurological Institute 152) (using settings in antsRegistrationSyN.sh) applied to the SE data and to the 1$^{st}$ echo of the ME data. These registrations were then used to map the 48 probabilistic cortical ROIs, "cortical ROIs", from the Harvard-Oxford Cortical Atlas and the 21 probabilistic subcortical ROIs, "subcortical ROIs", from the Harvard Oxford Subcortical Atlas to the QSM and $R_2$* template spaces.

The $T_1$-weighted MP2RAGE data was bias-field corrected, brain extracted, and segmented into five tissues using SPM (https://www.fil.ion.ucl.ac.uk/spm/): the grey matter (GM), white matter (WM) and cerebral-spinal fluid (CSF) volumes were mapped into each subject-specific QSM template space. Then, using "fslmaths" from FSL (https://fsl.fmrib.ox.ac.uk/fsl/), the mapped cortical ROIs were thresholded at 10% of the "robust range" of non-zero voxels and multiplied by the GM tissue map in order to obtain GM-specific cortical ROIs. The mapped subcortical ROIs were thresholded at 50% of the "robust range" of non-zero voxels. From these, any CSF voxels were

214 excluded from the left and right Caudate Nucleus, Putamen and Globus Pallidus, and
215 the voxel sets from the left and right counterparts were merged together.
216 From the SE and ME data, average $\chi$ and $R_2$* values were extracted from the manual
217 and Atlas-based ROIs for all volunteers and sessions in template space (values given in
218 Supplementary Material 1).
219 In order to estimate where the magnetic field is spatially more variable, field-maps
220 were first estimated from the ME datasets. $\Delta B_0$ was then calculated per-voxel as the
221 average difference between the field in a voxel and its immediate nearest neighbors.
222 The average $\Delta B_0$ was extracted for each of the cortical ROIs and averaged across all
223 subjects and sessions. Then the cortical ROIs were divided into two groups based on
224 the $\Delta B_0$ values: wherever $|\Delta B_0| > 0.005\ Hz$ the ROI was grouped into "high $\Delta B_0$"
225 regions, otherwise it was grouped into "low $\Delta B_0$" regions.
226 We explored three possible susceptibility reference regions for QSM processing. The
227 average QSM signal was extracted from:

228 1. A whole brain mask, "wb";
229 2. A whole-brain CSF mask eroded in two steps, "csf";
230 3. A manually placed cylindrical ROI in the right ventricle, "cyl" (across all subjects
231 the ROI volume was 104±11 $mm^3$).

232

233 ## 2.5. Statistical Analysis

234 Statistical analysis was performed with R 3.5.3 (R Core Team, 2013). Cross-site analysis
235 used only the 1st scan at the "home" site along with the scans at the other four sites.
236 To obtain the within subject average, $AV_w$, the $\chi$ and $R_2$* values were averaged within
237 the same site and across the sites and then averaged across subjects:

$$\mathrm{AV}_w = \frac{\sum_{i=1}^{m} (\sum_{j=1}^{n} x_{ij}/n)}{m} \qquad [1]$$

238 where $n$ is the number of sessions ($n = 5$ for within-site and cross-site) and $m$ the
239 number of subjects. Relative reliability was measured using the intra-class correlation
240 coefficient (ICC) from within and cross-site data independently for each ROI (Weir,
241 2005):

$$\mathrm{ICC} = \frac{MS_b - MS_w}{MS_b + MS_w(n-1)} \qquad [2]$$

where $MS_b$ and $MS_w$ are the between-subjects and within-subjects mean square from a random-effects, one-way analysis of variance (ANOVA) model. Intra-subject absolute variability is assessed by measuring the within-subject standard-deviation ($SD_w$) calculated as (Santin et al., 2017):

$$SD_w = \sqrt{\frac{\sum_{i=1}^{m} {\sigma_i}^2}{m}} \text{ with } \sigma_i = \frac{\sqrt{\sum_{j=1}^{n}(x_{ij} - \bar{x}_i)^2}}{n-1} \qquad [3]$$

where $\bar{x}_i = \sum_{j=1}^{n} x_{ij}/n$ is the replicate average for each subject. $SD_w$ was computed using within-site data and cross-site data independently. Similarly, cross-subject variability was calculated by measuring the between-subject standard-deviation ($SD_b$):

$$SD_b = \sqrt{\frac{\sum_{i=1}^{m}\sum_{j=1}^{n}(x_{ij} - x_{avg})^2}{n \times m - 1}} \qquad [4]$$

where $x_{avg} = \sum_{i=1}^{m}\sum_{j=1}^{n} x_{ij} \,/(n \times m)$ is the measurement average across subjects and sessions. Note that $SD_b$ is computed using data from all sites.

Statistical testing on $AV_w$, $SD_w$ and ICC values extracted from manual and template-based ROIs was done by first fitting the data with normal, log-normal, gamma and logistic distributions. The goodness-of-fit statistics for the parametric distributions were calculated and the distribution which showed the lowest Akaikes Information Criterion was then used on a general linear model fitting. All models included as fixed main effects ROI number and data type (within- and cross-site). When evaluating the data registration type, the model also included registration type ("Rigid" and "SyN") as a fixed main effect. When testing for QSM reference, the model also included reference region ("wb", "csf", and "cyl") as a fixed main effect. On ME QSM data, a model was fitted which also included the number of echoes processed as a fixed main effect. When comparing the manual and subcortical ROIs, the ROI type (manual vs. atlas-based) was also included as a fixed main effect. Finally, on the data from the cortical ROIs, ROI number was replaced with "high $\Delta B_0$" and "low $\Delta B_0$" ROI type as covariate. A p-value less than 0.05 was considered significant.

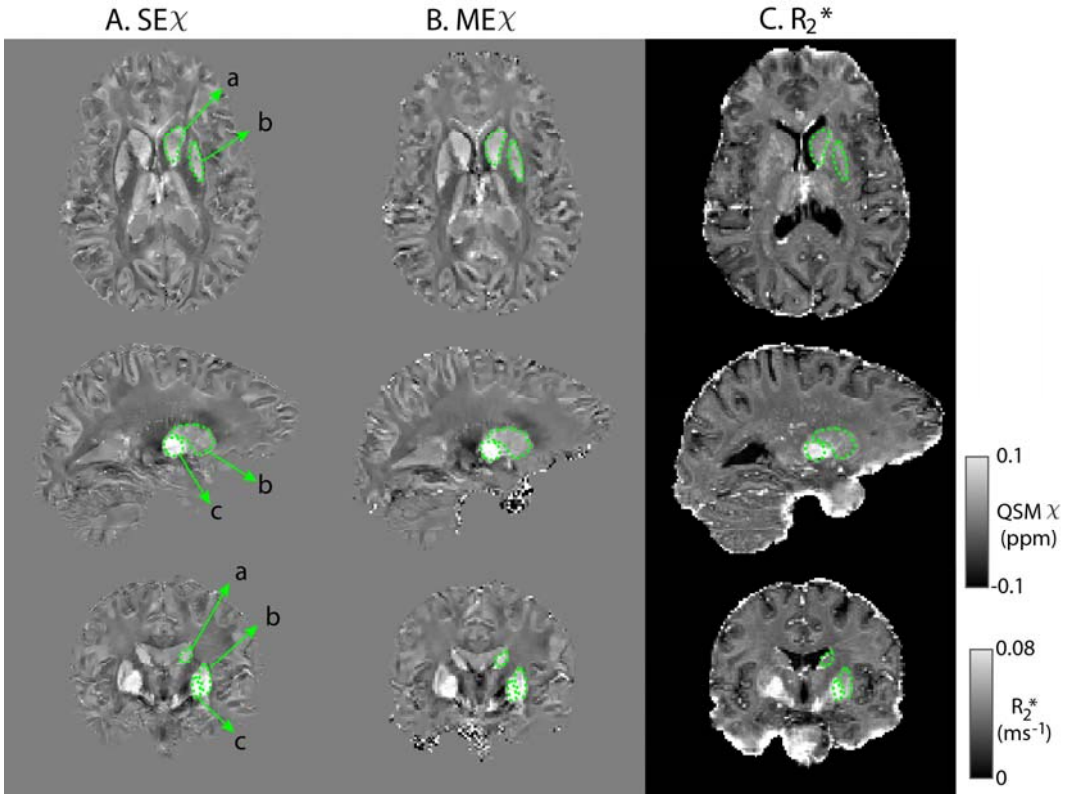


**Figure 1:** Representative slices of SE χ (A) ME χ (B) and $R_2$* maps (C) from an example subject. The right Caudate Nucleus (a), Putamen (b) and Globus Pallidus (c) are shown in green.

## 3. Results

Figure 1 shows QSM and $R_2$* maps for one example subject. Basal ganglia structures, including Caudate Nucleus, Putamen and Globus Pallidus are clearly visible consistent with previous findings (Langkammer et al., 2010; Wang et al., 2015; Betts et al., 2016; Acosta-Cabronero et al., 2016). Supplementary Material 2 Figure 1 highlights the difference in QSM data quality when using our chosen Roemer coil combination method *vs* using sum-of-squares coil combination.

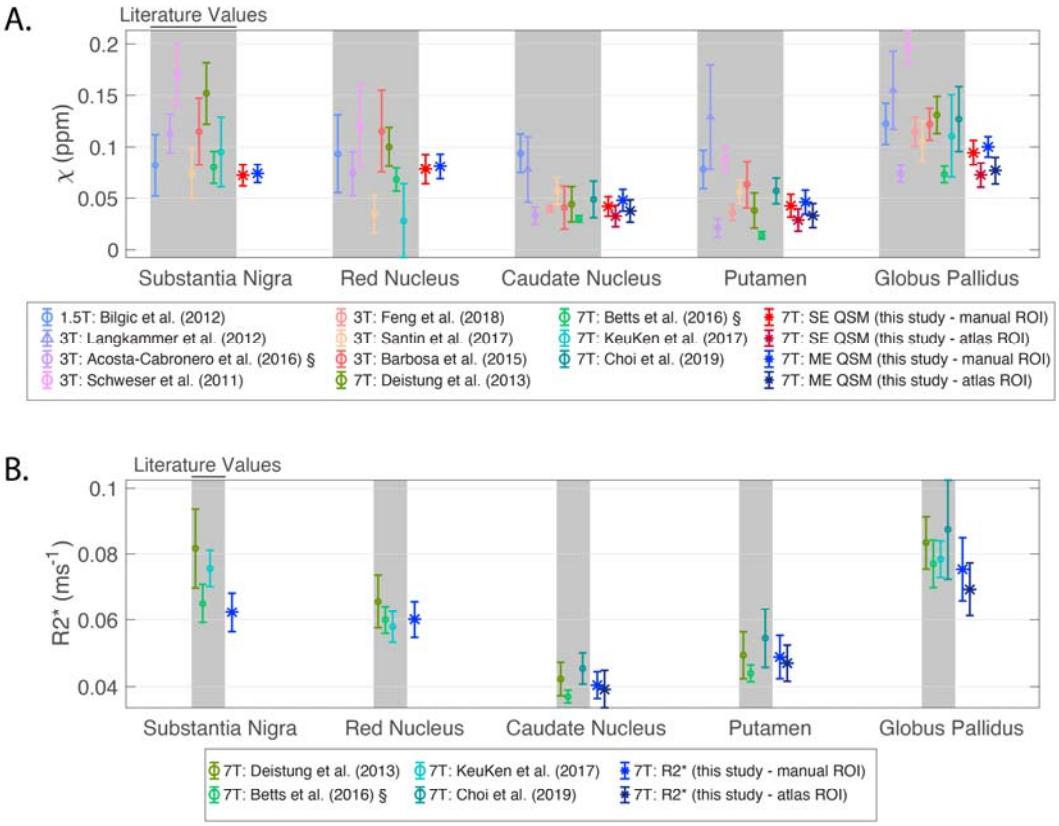


**Figure 2:** Mean and standard deviation literature values of QSM (A) and $R_2$* (B). The mean and standard deviation results from this study are also plotted. For data with the symbol '§' the standard error of the mean was originally reported and has been rescaled by reported N. Shaded regions correspond to literature data.

### 3.1. QSM and $R_2$* results and literature

Figure 2 compares average χ and $R_2$* values calculated in this study in the five manual ROIs and three corresponding atlas-based subcortical ROIs against literature ranges. The SE χ-values and ME χ-values from this study are consistent with literature values at 1.5T, 3T and 7T. $R_2$* values from this study also agree closely with 7T literature values.

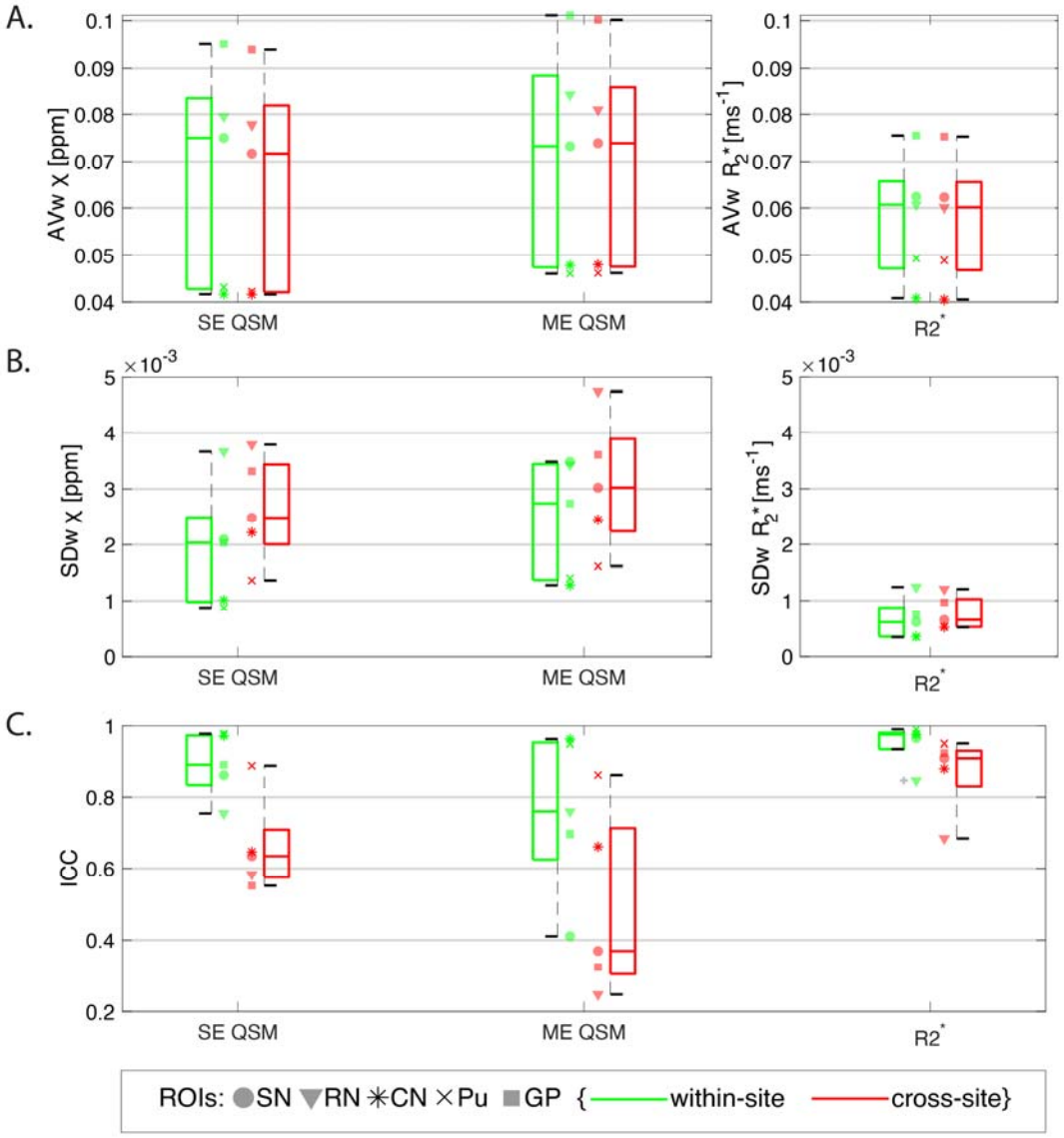


**Figure 3.** Boxplots from data obtained on the manual ROIs of within- and cross-site $AV_w$ (A), $SD_w$ (B) and ICC (C) of SE and ME QSM, and $R_2$*. Data from each ROI is shown with a different marker for each boxplot. Legend: SN=Substantia Nigra; RN: Red Nucleus; CN: Caudate Nucleus; Pu: Putamen; GP: Globus Pallidus.

### 3.2. Reproducibility of QSM and $R_2$*

Figure 3 shows boxplots over ROIs of the within- and cross-site $AV_w$ (A), $SD_w$ (B) and ICC (C) values for the manual ROIs on the χ and $R_2$* maps. The $AV_w$ from $R_2$* maps measured on the same site is systematically higher compared to the $AV_w$ measured across sites ($p < 0.0001$; e.g., on the Putamen ROI, $AV_{w\_within\text{-}site} = 0.0493$ ms$^{-1}$ vs $AV_{w\_cross\text{-}site} = 0.0489$ ms$^{-1}$). On this comparison, QSM data did not show significant

differences between within-site and cross-site groups for either SE data (p = 0.053) or ME data (p = 0.65).

From all the data in the manual ROIs, the median $SD_w$ of SE χ-values was approximately 29% lower than for ME χ-values (p = 0.0010). There was a significantly larger $SD_w$ cross-site compared to within-site on SE χ data (p < 0.0001; e.g., on the PN ROI, $SD_{w\_within\text{-}site}$ = 0.00088 ppm vs $SD_{w\_cross\text{-}site}$ = 0.0014 ppm), ME χ (p = 0.033) and on $R_2$* data (p < 0.0001).

The ICC values for within- and cross-site $R_2$* data (median ICC was 0.98 and 0.91, respectively) were found to be significantly higher than values for SE χ (median ICC was 0.89 and 0.64, respectively) or for ME χ (median was ICC 0.76 and 0.38, respectively) (p = 0.00011). For all measurements, the ICC for cross-site data was significantly lower than for within-site data (SE QSM: p < 0.0001; ME QSM: p = 0.017; $R_2$*: p < 0.0001).

Similar statistics were obtained for $AV_w$, $SD_w$ and ICC measurements in the altas-based cortical ROIs (Table 2, Supplementary Material 2).

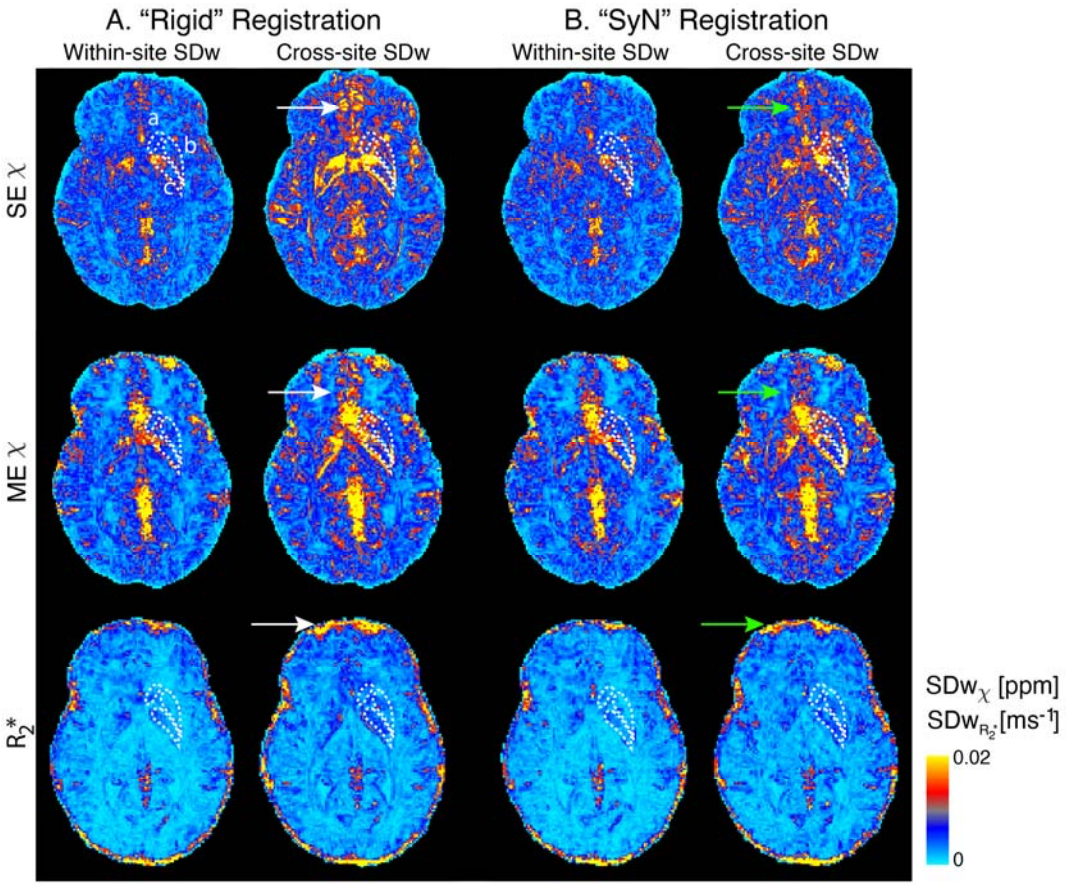

**Figure 4.** Voxel-wise within- and cross-site standard deviation of an example subject from SE and ME QSM and $R_2$* data with data registered with "Rigid" (A) and "SyN" (B) transformations. Arrows point to regions where the $SD_w$ decreased with the "SyN" transformations (green) are compared to "Rigid" (white). The right Caudate Nucleus (a), Putamen (b) and Globus Pallidus (c) are outlined in white.

### 3.3 Registration

The within- and cross-site standard deviations for one axial slice from one example subject using "Rigid" and "SyN" registration approaches are shown in Figure 4. Generally, with both registration methods, within-site and cross-site $SD_w$ increases in veins, in the orbitofrontal regions and at the cortical surface (white and green arrows, Figure 4). These are areas associated with large $B_0$ inhomogeneities and gradient non-linearity. However, there is a decrease in the cross-site standard deviation in the orbitofrontal region and close to the edges of the cortex when using the "SyN" compared to the "Rigid" method (green arrows, Figure 4).

On the manual ROIs increased variability was observed for $R_2$* on "Rigid" registered data compared to "SyN" ($SD_w$: $p < 0.0001$; ICC: $p < 0.013$) but not for SE or ME $\chi$: for example, the median cross-site $R_2$* $SD_w$ from all ROIs was 0.00066 $ms^{-1}$ using "SyN" method and 0.00086 $ms^{-1}$ using the "Rigid" registration method. On the atlas-based cortical ROIs, the same significant trend was observed for $R_2$* and SE $\chi$ data (Table 2, Supplementary Material 2).

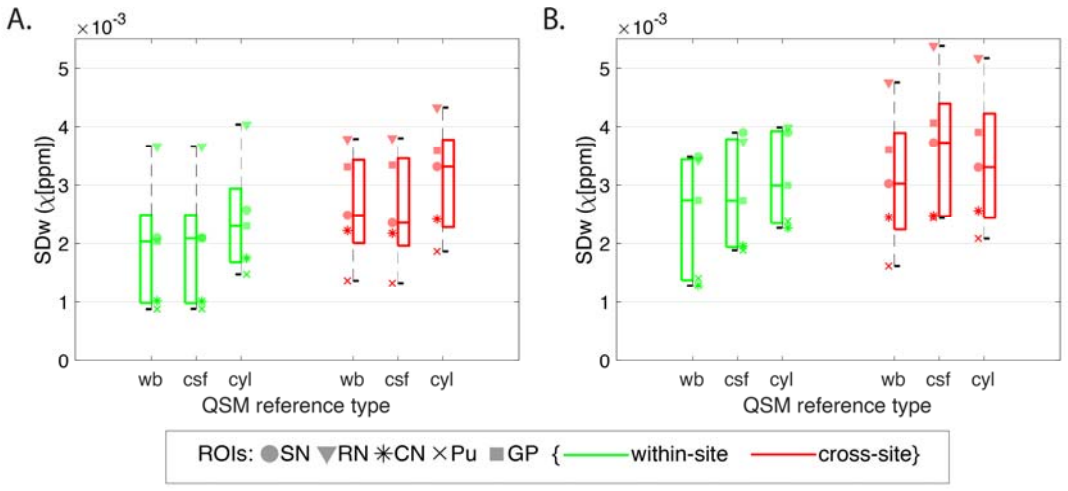


**Figure 5:** Boxplots from data obtained on the manual ROIs of within- and cross-site $SD_w$ (red and green, respectively) of SE QSM (A) and ME QSM (B) with a whole-brain reference (wb), with a csf reference (csf), and with a cylinder reference (cyl). Data from

each ROI is shown with a different marker for each boxplot. Legend: SN=Substantia Nigra; RN: Red Nucleus; CN: Caudate Nucleus; Pu: Putamen; GP: Globus Pallidus.

### 3.4 QSM referencing

To assess the optimal QSM susceptibility referencing, Figure 5 shows boxplots of the $SD_w$ for SE and ME χ using different referencing methods on the manual ROIs. On SE χ data, compared to "wb" correction (chosen correction for this study), the "csf" reference did not increase significantly the $SD_w$ ($p = 0.93$) but with "cyl" the median $SD_w$ increased by approximately 14% ($p < 0.0001$).

ME χ data showed an increase in the median $SD_w$ of, respectively, 11% ($p = 0.00096$) and 8% ($p = 0.00064$) when using "csf" and "cyl" methods for correction. The effect of varying the referencing of QSM data was similar in within-site and cross-site data, for all methods tested.

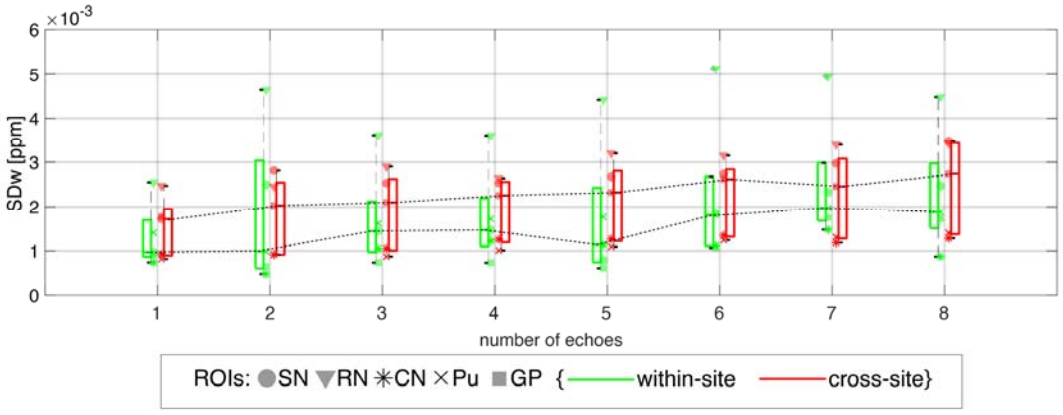


**Figure 6.** Boxplots from data obtained on the manual ROIs of within- and cross-site $SD_w$ for ME QSM calculated with different number of echoes. Increasing trend on the median $SD_w$ observed with increasing number of echoes (dotted lines). Legend: SN=Substantia Nigra; RN: Red Nucleus; CN: Caudate Nucleus; Pu: Putamen; GP: Globus Pallidus.

### 3.5 ME QSM

On average across all the manual ROIs and compared to single echo data, multi-echo data (using two or more echoes) showed a significant 14% increase of the $SD_w$ (Figure 6) and 3% of the ICC (Table 1, Supplementary Material 2). This supports the SE and ME χ comparison in Section 3.2. Similar behaviour was observed on the atlas-based cortical ROIs (Table 2, Supplementary Material 2). In the atlas-based cortical ROIs, long

echo times (i.e. using 6 or more echoes) showed an average increase of 15.7% in $SD_w$ ($p < 0.0001$) compared to using 2 to 5 echoes and a decrease of 1.75% in ICC ($p < 0.0001$) (Table 2, Supplementary Material 2).

### 3.6 ROI selection

There is a small but significant higher average $\chi$ from manually drawn ROIs compared to the atlas-based subcortical ROIs in SE QSM data ($p < 0.0001$; e.g. 0.042±0.009 ppm vs 0.033±0.010 ppm in the caudate nucleus) and in ME QSM data ($p < 0.0001$; e.g. 0.048±0.010 ppm vs 0.038±0.011 ppm in the caudate nucleus) (Figure 2). Similarly, for $R_2$* (e.g. 0.041±0.004 $ms^{-1}$ vs 0.039±0.006 $ms^{-1}$ in the caudate nucleus) this difference was significant ($p < 0.0001$). In addition, the $SD_w$ was, on average, approximately two times higher and the ICC lower in the atlas-based subcortical ROIs compared to the manual ROIs in all datasets ($SD_w$: SE QSM $p < 0.0001$, ME QSM $p < 0.0001$, $R_2$* $p < 0.0001$; ICC: SE QSM $p = 0.00021$, ME QSM $p = 0.0023$, $R_2$* $p = 0.012$). So, ROI selection should be done consistently in a study.

### 3.7 Spatial distribution of the magnetic field

On the altas-based cortical ROIs the $SD_w$ increased by approximately 28% and 88% on "high $\Delta B_0$" regions compared to "low $\Delta B_0$" regions on ME $\chi$ and $R_2$* data, respectively ($p = 0.0011$ and $p < 0.0001$) (Table 2, Supplementary Material 2). Similarly, ICC values decreased significantly for SE and ME $\chi$ and $R_2$* values.

## 4. Discussion

In this paper, the reproducibility of QSM $\chi$ and $R_2$* measurements in cortical and subcortical regions of the brain was assessed for the first time in a multi-site study at 7T for two different protocols (a single-echo 0.7mm isotropic $T_2$*-weighted scan and a 1.5mm isotropic multi-echo $T_2$*-weighted scan), using three different scanner platforms provided by two different vendors.

Previous studies at 1.5T and 3T have shown good reproducibility for $\chi$ and $R_2$* data acquired on the same scanner or across sites (1.5T and 3T) (Hinoda et al., 2015; Cobzas et al., 2015; Deh et al., 2015; Lin et al., 2015; Santin et al., 2017; Feng et al., 2018;

Spincemaille et al., 2019). In terms of QSM and depending on the subcortical region, intra-scanner 3T repeatability studies report an $SD_w$ of 0.002-0.005 ppm (Feng et al., 2018) and 0.004-0.006 ppm (Santin et al., 2017), and the cross-site 3T study by Lin et al. (2015) reported an average $SD_W$ of 0.006-0.010 ppm. We observed a within-site $SD_w$ range of 0.0009-0.004 ppm and cross-site $SD_w$ range of 0.001-0.005 ppm at 7T. The latter is therefore 21-95% better than within sites studies at 3T.

The range of within-site $SD_w$ values for $R_2$* was averaged 0.0003-0.001 $ms^{-1}$ in our study and the cross-site $SD_w$ range was 0.0005-0.001 $ms^{-1}$. The cross-site values are comparable to the *same site* reported at 3T: 0.0005-0.0009 $ms^{-1}$ (Feng et al., 2018), 0.0006-0.002 $ms^{-1}$ (Santin et al., 2017). Compared to the latter, our cross-site results show a reduction of 15-124% in $R_2$* variability.

The higher values of cross-site $SD_w$ compared to the within-site values in our study may be attributed to the different gradient systems and automatic distortion corrections used in the different scanner platforms and to the different approaches to shimming, which lead to different geometrical distortions and dropout regions (Yang et al., 2010). We showed that the use of a non-linear registration method (here, "SyN" in ANTs) significantly reduced the inter-scanner variability of cortical QSM compared to rigid-body registration, indicating that differences in geometric distortion across scanners were present. The $R_2$* results for both cortical and subcortical structures also show significantly lower inter-scanner variability when a non-linear registration was used.

In this study, the reproducibility of QSM using single-echo (SE), high-resolution (0.7 mm isotropic resolution; TE=20ms) and multi-echo standard-resolution (ME) standard-resolution (1.4 mm isotropic resolution; TE=4, 9, 14, 19, 24, 29, 34 and 39 ms) protocols were compared, and the results show that the ME QSM data has a significantly higher variability than SE QSM. Although ME QSM data has been combined with a magnitude-weighted least squares regression of phase to echo time, it may carry incorrect phase from late echoes of the echo train that suffered multiple phase wraps. This has also been verified with an analysis on multi-echo QSM data reconstructed with different numbers of echoes: long echo times increase significantly the test-retest variability.

$R_2$* values show significantly lower variability, reflected in the higher ICC within and across-sites compared to corresponding values for $\chi$ in subcortical areas. This may be because the $\chi$ estimation is globally more sensitive to background field inhomogeneity compared to magnitude data. However, in orbitofrontal and lower temporal regions large through-plane field variations from tissue-air interfaces dominate the field changes and produce dropouts in the signal magnitude and increase the background phase, affecting both QSM and $R_2$* maps by increasing variability and decreasing ICC.

QSM can only determine relative susceptibility differences (Cheng et al., 2009) and most approaches to calculation of susceptibility from measured phase yield maps in which the average value of susceptibility is zero over the masked imaging volume. Issues related to referencing of QSM data have been investigated (Feng et al., 2018; Straub et al., 2017), with aim of finding a reference region or tissue to which all susceptibility values are referred that produces well-defined and reproducible values of susceptibility. Here we investigated how the choice of reference affects the within-site and cross-site variability of measured susceptibility at ultra-high-field. We tested three accepted reference regions: total whole brain signal, “wb”, whole brain CSF eroded in order to exclude any pial or skull surfaces, “csf”, and a manually selected cylindrical ROI in the right ventricle, “cyl”. We found that the “cyl” referencing generally increased the variability of the cross-site and within-site susceptibility measurements in cortical and subcortical ROIs compared to “wb” referencing. In the case of ME acquisition the “csf” referencing also increased the variability relative to “wb” data. This may be because of imprecision in systematically obtaining average QSM signal from CSF regions. Referencing using a small ROI in the ventricles might be prone to subjectivity given the natural variation in ventricle size in healthy subjects and in disease. Furthermore, the ventricles do not contain pure CSF: they are traversed by blood vessels with a different $\chi$ (Sullivan et al., 2002). This makes whole-brain referencing attractive in many situations. Yet, in patient cohorts where there is substantial iron load in subcortical structures (Snyder and Connor, 2009), whole brain referencing might not be an appropriate approach. In this case, the more appropriate approach will be to choose a small reference region which shows no changes in the particular disease to be “zero” susceptibility at a cost of a slight increase in SD.

462

463 To eliminate operator-dependent bias in segmentation when determining brain
464 structures, we have analysed data using both manual and atlas-based segmentation.
465 From our results, manual ROIs showed significantly lower variability compared to atlas-
466 based methods. This happens because of imprecision in registration between MNI and
467 subject space as well as the empirical thresholding that was chosen to obtain the
468 subcortical ROIs. However, traditional manual drawing of ROIs for cohort studies is
469 difficult, time consuming and potentially unsuitable as it biases results towards
470 particular cohorts (Collins et al., 2003) so it may not always be the most appropriate
471 approach.

472

473 In this study, harmonized protocols were produced for all five scanners without any
474 significant sequence alterations, as a product 3D gradient echo (GE) sequence was
475 readily available on all systems (the product 'gre' sequence from Siemens and the
476 product 'ffe' from Philips). The protocols and an example dataset are provided in
477 (Clarke, 2018). Generally, we also relied on the vendors' reconstruction. However, at
478 the end of the reconstruction pipeline of the Siemens systems we adopted a different
479 coil combination approach based on Roemer et al. (1990) and Walsh et al. (2000), to
480 match the SENSE approach implemented on Philips scanners (Pruessmann et al., 1999;
481 Robinson et al., 2017). This was required due to artifacts appearing on phase images in
482 Siemens data reconstructed with the vendor's pipeline, such as open-ended fringe
483 lines or singularities (Chavez et al., 2002) (Figure 1, Supplementary Material 2). These
484 reduce the consistency of the QSM results (Santin et al., 2017). However, other coil
485 combination methods such as a selective channel combination approach (Vegh et al.,
486 2016) or the COMPOSER (COMbining Phase data using a Short Echo-time Reference
487 scan) method (Bollmann et al., 2018) have also been shown to reduce open-ended
488 fringe lines and noise in the signal phase. For future investigations, the raw k-space
489 data collected from all sites in this study has been stored and is available from the
490 authors upon request.

491

492 On the QSM reconstruction, an imperfect background field filtering can influence the
493 reproducibility of QSM data. For this reason, we performed background removal in

two steps as implemented in QSMbox v2.0 and as described in (Acosta-Cabronero et al., 2018): first with the LBV approach and then followed by the vSMV method. Regularized field-to-susceptibility inversion strategies have been proposed to overcome the ill-posed problem in QSM with data acquired at a single head orientation (de Rochefort et al., 2010). We opted to use the MSDI implementation in QSMbox v2.0 (Acosta-Cabronero et al., 2018), as it ranked top-10 in all metrics of the 2016 QSM Reconstruction Challenge (Langkammer et al., 2018), and also now includes a new self-optimized local scale, which results in a better preservation of phase noise texture and low susceptibility contrast features. On the second step, the regularization factor, λ, used for this study was set to $10^{2.7}$, as recommended by Acosta-Cabronero et al. (2018) based on an L-curve analysis (Hansen et al., 1993) with high-resolution 7T data.

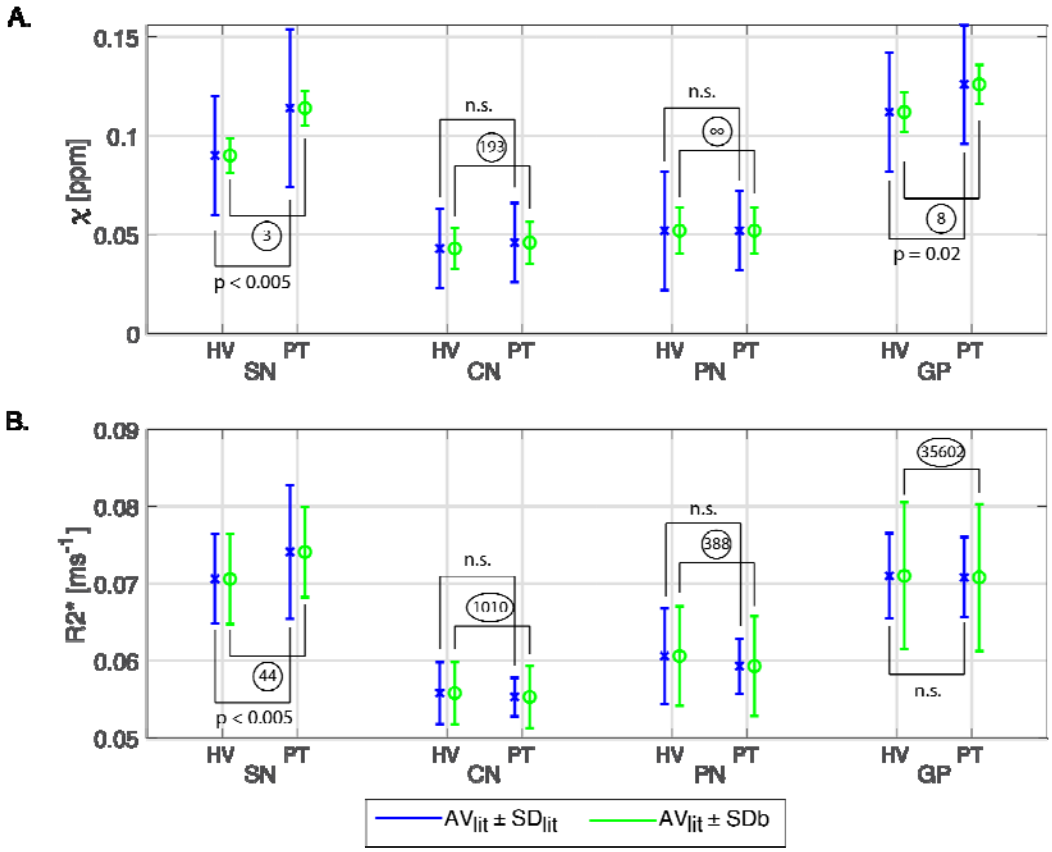


**Figure 7.** Illustration of the feasibility of a 7T QSM clinical study. χ (A) and $R_2$* (B) for four ROIs (Substantia Nigra, SN; Caudate Nucleus, CN; Putamen, Pu; Globus Pallidus, GP) from healthy volunteer (HV) and synthetic "patient" (PT) data for which $AV_{lit}$ and $SD_{lit}$ were obtained from Langkammer et al. (2016) and $SD_b$ were calculated from data of the current study. $AV_{lit}$ values for $R_2$* were linearly scaled to 7T according to Yao et al. (2007). Blue bars show the $AV_{lit} \pm SD_{lit}$ and green bars the $AV_{lit} \pm SD_b$. Statistical

differences between HV and PT obtained from Langkammer et al. (2016) are also shown. For each ROI, the sample size that would have been needed to give a significant effect was calculated from the group means, $AV_{lit}$, and the $SD_b$ per ROI and is shown in circles.

To minimise confounding effects of age or pathology, we assessed test-retest reliability and cross-site variability with ten healthy young subjects. The cross-site, between-subject standard-deviation, $SD_b$, measured in this study was evaluated together with healthy and Parkinson's disease data from (Langkammer et al., 2016). A power analysis revealed a sample size that would have been required for a multi-site clinical study in each ROI as shown in Figure 7. For all the significant ROIs the number of subjects that would have been required per group was less or equal to 44. Since this is lower than the sample size we have used in this study (90 healthy volunteer scans) and the numbers in the Langkammer study (66 patients and 58 control subjects), it gives strong confidence of feasibility for future 7T QSM clinical studies.

## 5. Conclusion

We investigated test-retest reliability and reproducibility of $T_2$*-weighted imaging protocols at ultra-high field MRI. Considering the increase in susceptibility effects at 7T, we found that variability of measurements of QSM $\chi$ and $R_2$* in the basal ganglia are reduced compared to reports from lower field strengths, 1.5T and 3T. Scanner hardware differences give more modest improvements for cortical measurements of QSM $\chi$ and $R_2$*. Multi-echo protocols do not benefit from long echo times as these increase the imprecision in the estimation of QSM. We suggest that 7T MRI is suitable for multicentre quantitative analyses of brain iron, in health and disease.

## 6. Acknowledgements

The UK7T Network and this work was funded by the UK's Medical Research Council (MRC) [MR/N008537/1]. We thank Julio Acosta-Cabronero for making the QSMbox publically available.

## 7. Centre funding

The Wellcome Centre for Integrative Neuroimaging is supported by core funding from the Wellcome Trust (203139/Z/16/Z).

Cardiff University Brain Research Imaging Centre is supported by the UK Medical Research Council (MR/M008932/1) and the Wellcome Trust (WT104943).

This research was co-funded by the NIHR Cambridge Biomedical Research Centre. The views expressed are those of the author(s) and not necessarily those of the NHS, the NIHR or the Department of Health and Social Care. The Cambridge 7T MRI facility is co-funded by the University of Cambridge and the Medical Research Council (MR/M008983/1).

## 8. Individual funding

CTR is funded by a Sir Henry Dale Fellowship from the Wellcome Trust and the Royal Society [098436/Z/12/B]. JBR is supported by the Wellcome Trust (WT103838).

## 9. References

Abdul-Rahman, H., Gdeisat, M., Burton, D., Michael, L., 2005. Fast three-dimensional phase-unwrapping algorithm based on sorting by reliability following a non-continuous path. App. Optic. 46, 6623-6635. https://doi.org/10.1117/12.611415

Acosta-Cabronero, J., Milovic, C., Mattern, H., Tejos, C., Speck, O., Callaghan, M.F., 2018. A robust multi-scale approach to quantitative susceptibility mapping. NeuroImage 183, 7-24. https://doi.org/10.1016/j.neuroimage.2018.07.065

Acosta-Cabronero, J., Betts, M.J., Cardenas-Blanco, A., Yang, S., Nestor, P.J., 2016. In Vivo MRI mapping of brain iron deposition across the adult lifespan. J. Neurosci. 36, 364–374. https://doi.org/10.1523/JNEUROSCI.1907-15.2016

Acosta-Cabronero, J., Williams, G.B., Cardenas-Blanco, A., Arnold, R.J., Lupson, V., Nestor, P.J., 2013. In vivo quantitative susceptibility mapping (QSM) in Alzheimer's disease. PLoS One 8, e81093. https://doi.org/10.1371/journal.pone.0081093

Barbosa, J.H.O., Santos, A.C., Salmon, C.E.G., 2015. Susceptibility weighted imaging: differentiating between calcification and hemosiderin. Radiologia brasileira 48(2), 93-100. https://doi.org/10.1590/0100-3984.2014.0010

Betts, M.J., Acosta-Cabronero, J., Cardenas-Blanco, A., Nestor, P.J. and Düzel, E., 2016. High-resolution characterisation of the aging brain using simultaneous quantitative susceptibility

mapping (QSM) and R2* measurements at 7 T. Neuroimage 138, pp.43-63. https://doi.org/10.1016/j.neuroimage.2016.05.024

Bilgic, B., Pfefferbaum, A., Rohlfing, T., Sullivan, E.V., Adalsteinsson, E., 2012. MRI estimates of brain iron concentration in normal aging using quantitative susceptibility mapping. Neuroimage 59(3), 2625-2635. https://doi.org/10.1016/j.neuroimage.2011.08.077

Blazejewska, A.I., Al-Radaideh, A.M., Wharton, S., Lim, S.Y., Bowtell, R.W., Constantinescu, C.S., Gowland, P.A., 2015. Increase in the iron content of the substantia nigra and red nucleus in multiple sclerosis and clinically isolated syndrome: a 7 Tesla MRI study. J. Magn. Reson. Imaging 41, 1065-1070. https://doi.org/10.1002/jmri.24644

Bollmann, S., Robinson, S.D., O'Brien, K., Vegh, V., Janke, A., Marstaller, L., Reutens, D., Barth, M., 2018. The challenge of bias-free coil combination for quantitative susceptibility mapping at ultra-high field. Magn. Reson. Med. 79(1), 97-107. https://doi.org/10.1002/mrm.26644

Chavez, S., Xiang, Q., Li, A., 2002. Understanding phase maps in MRI: a new cutline phase unwrapping method. IEEE Trans Med Imaging 21, 966–977. https://doi.org/10.1109/TMI.2002.803106

Cheng, Y.-C.N., Neelavalli, J., Haacke, E.M., 2009. Limitations of calculating field distributions and magnetic susceptibilities in MRI using a Fourier based method. Phys. Med. Biol. 54(5), 1169–1189. https://doi.org/10.1088/0031-9155/54/5/005

Choi, S., Li, X., Harrison, D.M., 2019. The impact of coregitration of gradient recalled echo images on quantitative susceptibility and R2* mapping at 7T. bioRxiv. https://doi.org/10.1101/529891

Clarke, W.T., 2018. UK7T Network harmonized neuroimaging protocols. https://ora.ox.ac.uk/objects/uuid:55ca977f-62df-4cbf-b300-2dc893e36647.

Clarke, W.T., Mougin, O., Driver, I.D., Rua, C., Morgan, A., Asghar, M., Clare, S., Francis, S., Wise, R., Rodgers, C.T., Carpenter, T.A., Muir, K., Bowtell, R., 2019. Multi-site harmonization of 7 Tesla MRI neuroimaging protocols. NeuroImage 206, 116335. https://doi.org/10.1016/j.neuroimage.2019.116335

Cobzas, D., Sun, H.F., Walsh, A.J., Lebel, R.M., Blevins, G., Wilman, A.H., 2015. Subcortical gray matter segmentation and voxel-based analysis using transverse relaxation and quantitative susceptibility mapping with application to multiple sclerosis. J. Magn. Reson. Imaging 42(6), 1601–1610. https://doi.org/10.1002/jmri.24951

Collins, D.L., Zijdenbos, A.P., Paus, T., Evans, A.C., 2003. Use of registration for cohort studies. Medical image registration.

de Rochefort, L., Liu, T., Kressler, B., Liu, J., Spincemaille, P., Lebon, V., Wu, J., Wang, Y., 2010. Quantitative susceptibility map reconstruction from MR phase data using Bayesian regularization: validation and application to brain imaging. Magn. Reson. Med. 63, 194–206. https://doi.org/10.1002/mrm.22187

Deh, K., Nguyen, T.D., Eskreis-Winkler, S., Prince, M.R., Spincemaille, P., Gauthier, S., Kovanlikaya, I., Zhang, Y., Wang, Y., 2015. Reproducibility of quantitative susceptibility mapping in the brain at two field strengths from two vendors. J. Magn. Reson. Imaging 42, 1592–1600. https://doi.org/10.1002/jmri.24943

617 Deistung, A., Schäfer, A., Schweser, F., Biedermann, U., Güllmar, D., Trampel, R., Turner, R.,
618 Reichenbach, J.R., 2013. High-resolution MR imaging of the human brainstem in vivo at 7
619 Tesla. Frontiers in human neuroscience 7, 710. https://doi.org/10.3389/fnhum.2013.00710

620 Duyn, J.H., van Gelderen, P., Li, T.Q., de Zwart, J.A., Koretsky, A.P. and Fukunaga, M., 2007.
621 High-field MRI of brain cortical substructure based on signal phase. Proceedings of the
622 National Academy of Sciences, 104(28), pp.11796-11801.
623 https://doi.org/10.1073/pnas.0610821104

624 Ehses, P., Brenner, D., Stirnberg, R., Pracht, E.D., Stöcker, T., 2019. Whole-brain B1-mapping
625 using three-dimensional DREAM. Magn. Reson. Med. 82(3), 924-934.
626 https://doi.org/10.1002/mrm.27773

627 Eskreis-Winkler, S., Zhang, Y., Zhang, J., Liu, Z., Dimov, A., Gupta, A. and Wang, Y., 2017. The
628 clinical utility of QSM: disease diagnosis, medical management, and surgical planning. NMR in
629 Biomedicine 30(4), p.e3668. https://doi.org/10.1002/nbm.3668

630 Feng, X., Deistung, A., Reichenbach, J.R., 2018. Quantitative susceptibility mapping (QSM) and
631 R2* in the human brain at 3 T: Evaluation of intra-scanner repeatability. Z. Med. Phys. 28, 36–
632 48. https://doi.org/10.1016/j.zemedi.2017.05.003

633 Gelman, N., Gorell, J.M., Barker, P.B., Savage, R.M., Spickler, E.M., Windham, J.P., Knight, R.A.,
634 1999. MR imaging of human brain at 3.0 T: preliminary report on transverse re-laxation rates
635 and relation to estimated iron content. Radiology 210, 759–767.
636 https://doi.org/10.1148/radiology.210.3.r99fe41759

637 Haacke, E.M., Cheng, N., House, M.J., Liu, Q., Neelavalli, J., Ogg, R.J., Khan, A., Ayaz, M., Kirsch,
638 W., Obenaus, A., 2005. Imaging iron stores in the brain using magnetic resonance imaging.
639 Magn. Reson. Imag. 23, 1-25. https://doi.org/10.1016/j.mri.2004.10.001

640 Hansen, P.C., O'Leary, D.P., 1993. The use of the l-curve in the regularization of discrete ill-
641 posed problems. SIAM J Sci Comput 14(6), 1487-1503. https://doi.org/10.1137/0914086

642 He, X., Yablonskiy, D.A., 2009. Biophysical mechanisms of phase contrast in gradient echo MRI.
643 Proc. Natl. Acad. Sci. U.S.A. 106, 13558–13563. https://doi.org/10.1073/pnas.0904899106

644 Hinoda, T., Fushimi, Y., Okada, T., Fujimoto, K., Liu, C., Yamamoto, A., Okada, T., Kido, A.,
645 Togashi, K., 2015. Quantitative susceptibility mapping at 3 T and 1.5 T: evaluation of
646 consistency and reproducibility. Invest. Radiol. 50, 522-530.
647 https://doi.org/10.1097/RLI.0000000000000159

648 House, M.J., Pierre, T.G.S., Kowdley, K.V., Montine, T., Connor, J., Beard, J., Berger, J., Siddaiah,
649 N., Shankland, E., Jin, L.W., 2007. Correlation of proton transverse relaxation rates (R2) with
650 iron concentrations in postmortem brain tissue from Alzheimer's disease patients. Magn.
651 Reson. Med. 57, 172–180. https://doi.org/10.1002/mrm.21118

652 Keuken, M.C., Bazin, P.L., Backhouse, K., Beekhuizen, S., Himmer, L., Kandola, A., Lafeber, J.J.,
653 Prochazkova, L., Trutti, A., Schäfer, A., Turner, R., 2017. Effects of aging on T1, T2∗, and QSM
654 MRI values in the subcortex. Brain Structure and Function 222(6), 2487-2505.
655 https://doi.org/10.1007/s00429-016-1352-4

Lancione, M., Tosetti, M., Donatelli, G., Cosottini, M., Costagli, M., 2017. The impact of white matter fiber orientation in single-acquisition quantitative susceptibility mapping. NMR Biomed. 30, e3798. https://doi.org/10.1002/nbm.3798

Langkammer, C., Schweser, F., Shmueli, K., Kames, C., Li, X., Guo, L., Milovic, C., Kim, J., Wei, H., Bredies, K., Buch, S., 2018. Quantitative susceptibility mapping: report from the 2016 reconstruction challenge. Magn. Reson. Med. 79(3), 1661-73. https://doi.org/10.1002/mrm.26830

Langkammer, C., Pirpamer, L., Seiler, S., Deistung, A., Schweser, F., Franthal, S., Homayoon, N., Katschnig-Winter, P., Koegl-Wallner, M., Pendl, T., Stoegerer, E.M., 2016. Quantitative susceptibility mapping in Parkinson's disease. PLoS One, 11(9), e0162460. https://doi.org/10.1371/journal.pone.0162460

Langkammer, C., Schweser, F., Krebs, N., Deistung, A., Goessler, W., Scheurer, E., Sommer, K., Reishofer, G., Yen, K., Fazekas, F., Ropele, S., Reichenbach, J.R., 2012. Quantitative susceptibility mapping (QSM) as a means to measure brain iron? A post mortem validation study. Neuroimage 62(3), 1593–1599. https://doi.org/10.1016/j.neuroimage.2012.05.049

Langkammer, C., Krebs, N., Goessler, W., Scheurer, E., Ebner, F., Yen, K., Fazekas, F., Ropele, S., 2010. Quantitative MR imaging of brain iron: a postmortem validation study. Radiology 257(2), 455-462. https://doi.org/10.1148/radiol.10100495

Lee, J., Shmueli, K., Kang, B.T., Yao, B., Fukunaga, M., van Gelderen, P., Palumbo, S., Bosetti, F., Silva, A.C., Duyn, J.H., 2012. The contribution of myelin to magnetic susceptibility-weighted contrasts in high-field MRI of the brain. Neuroimage 59, 3967–3975. https://doi.org/10.1016/j.neuroimage.2011.10.076

Li, G., Zhai, G., Zhao, X., An, H., Spincemaille, P., Gillen, K.M., Ku, Y., Wang, Y., Huang, D., Li, J., 2019. 3D texture analysis within substantia nigra of Parkinson's disease patients on quantitative susceptibility maps and R2* maps. NeuroImage 188, 465-472. https://doi.org/10.1016/j.neuroimage.2018.12.041

Li, L., Leigh, J.S., 2004. Quantifying arbitrary magnetic susceptibility distributions with MR. Magn. Reson. Med. 51, 1077–1082. https://doi.org/10.1002/mrm.20054

Li, W., Liu, C., Duong, T.Q., van Zijl, P.C., Li, X., 2017. Susceptibility tensor imaging (STI) of the brain. NMR Biomed. 30(4), p.e3540. https://doi.org/10.1002/nbm.3540

Lin, P.Y., Chao, T.C., Wu, M.L., 2015. Quantitative susceptibility mapping of human brain at 3T: a multisite reproducibility study. AJNR Am J. Neuroradiol. 36, 467-474. https://doi.org/10.3174/ajnr.A4137

Lotfipour, A.K., Wharton, S., Schwarz, S.T., Gontu, V., Schaefer, A., Peters, A.M., Bowtell, R.W., Auer, D.P., Gowland, P.A., Bajaj, P.S., 2012. High resolution magnetic susceptibility mapping of the substantia nigra in Parkinson's disease. J. Magn. Reson. Imag. 35, 48-55. https://doi.org/10.1002/jmri.22752

Mougin, O., Clarke, W., Driver, I., Rua, C., Morgan, A.T., Francis, S., Muir, K., Carpenter, A., Rodgers, C., Wise, R., Porter, D., Clare, S., Bowtell, R., 2019. Robustness of PSIR segmentation and R1 mapping at 7T: a travelling head study. Proc. Intr. Soc. Mag. Reson. Med. 27, 237.

696 Nehrke, K., Bornert, P., 2012. DREAM--a novel approach for robust, ultrafast, multislice B(1)
697 mapping. Magn. Reson. Med. 68(5), 1517-1526. https://doi.org/10.1002/mrm.24158

698 Pei, M., Nguyen, T.D., Thimmappa, N.D., Salustri, C., Dong, F., Cooper, M.A., Li, J., Prince, M.R.,
699 Wang, Y., 2015. Algorithm for fast monoexponential fitting based on auto-regression on linear
700 operations (ARLO) of data. Magn. Reson. Med. 73, 843-850.
701 https://doi.org/10.1002/mrm.25137

702 Pruessmann, K.P., Weiger, M., Scheidegger, M.B., Boesiger, P., 1999. SENSE: sensitivity
703 encoding for fast MRI. Magn. Reson. Med. 42(5), 952-962. https://doi.org/10.1002/(SICI)1522-
704 2594(199911)42:5<952::AID-MRM16>3.0.CO;2-S

705 R Core team, 2013. R: A language and environment for statistical computing. R Foundation for
706 Statistical Computing, Vienna, Austria. http:// www.R-project.org/.

707 Reichenbach, J.R., 2012. The future of susceptibility contrast for assessment of anatomy and
708 function. Neuroimage 62, 1311-1315. https://doi.org/10.1016/j.neuroimage.2012.01.004

709 Reichenbach, J.R., Jonetz-Mentzel, L., Fitzek, C., Haacke, E.M., Kido, D.K., Lee, B.C., Kaiser,
710 W.A., 2001. High-resolution blood oxygen-level dependent MR venography (HRBV): a new
711 technique. Neuroradiology 43, 364–369. https://doi.org/10.1007/s002340000503

712 Robinson, S.D., Bredies, K., Khabiova, D., Dymerska, B., Marques, J.P., Schweser, F., 2017. An
713 illustrated comparison of processing methods for MR phase imaging and QSM: combining
714 array coil signals and phase unwrapping. NMR Biomed. 30, e3601.
715 https://doi.org/10.1002/nbm.3601

716 Roemer, P.B., Edelstein, W.A., Hayes, C.E., Souza, S.P., Mueller, O.M., 1990. The NMR phased
717 array. Magn. Reson. Med. 16(2), 192-225. https://doi.org/10.1002/mrm.1910160203

718 Santin, M.D., Didier, M., Valabregue, R., Yahia Cherif, L., García-Lorenzo, D., Loureiro de Sousa,
719 P., Bardinet, E., Lehéricy, S., 2017. Reproducibility of R2* and quantitative susceptibility
720 mapping (QSM) reconstruction methods in the basal ganglia of healthy subjects. NMR Biomed.
721 30(4), e3491. https://doi.org/10.1002/nbm.3491

722 Schweser, F., Deistung, A., Lehr, B.W., Reichenbach, J.R., 2011. Quantitative imaging of intrinsic
723 magnetic tissue properties using MRI signal phase: an approach to in vivo brain iron
724 metabolism?. Neuroimage 54(4), 2789-2807.
725 https://doi.org/10.1016/j.neuroimage.2010.10.070

726 Smith, S.M., 2002. Fast robust automated brain extraction. Human Brain Mapping 17(3), 143-
727 155. https://doi.org/10.1002/hbm.10062

728 Snyder A.M., Connor J.R., 2009. Iron, the substantia nigra and related neurological disorders.
729 Biochimica et Biophysics Acta 1790, 606-614. https://doi.org/10.1016/j.bbagen.2008.08.005

730 Spincemaille, P., Liu, Z., Zhang, S., Kovanlikaya, I., Ippoliti, M., Makowski, M., Watts, R., de
731 Rochefort, L., Venkatraman, V., Desmond, P. and Santin, M.D., 2019. Clinical integration of
732 automated processing for brain quantitative susceptibility mapping: multi-site reproducibility
733 and single-site robustness. Journal of Neuroimaging, 29(6), pp.689-698.
734 https://doi.org/10.1111/jon.12658

735 Straub, S., Schneider, T.M., Emmerich, J., Freitag, M.T., Ziener, C.H., Schlemmer, H.P., Ladd,
736 M.E., Laun, F.B., 2017. Suitable reference tissues for quantitative susceptibility mapping of the
737 brain. Magn. Reson. Med. 78, 204-214. https://doi.org/10.1002/mrm.26369

738 Sullivan, E.V., Pfefferbaum, A., Adalsteinsson, E., Swan, G.E., Carmelli, D., 2002. Differential
739 rates of regional brain change in callosal and ventricular size: a 4-year longitudinal MRI study
740 of elderly men. Cereb. Cortex 12(4), 438-45. https://doi.org/10.1093/cercor/12.4.438

741 Tie-Qiang, T., Gelderen, P., Merkle, H., Talagala, L., Koretsky, A.P., Duyn, J., 2006. Extensive
742 heterogeneity in white matter intensity in high-resolution T2*-weighted MRI of the human
743 brain at 7.0 T. NeuroImage 32, 1032-1040. https://doi.org/10.1016/j.neuroimage.2006.05.053

744 Vegh, V., O'Brien, K., Barth, M. and Reutens, D.C., 2016. Selective channel combination of MRI
745 signal phase. Magn. Reson. Med. 76(5), 1469-1477. https://doi.org/10.1002/mrm.26057

746 Walsh, D.O., Gmitro, A.F., Marcellin, M.W., 2000. Adaptive reconstruction of phased array MR
747 imagery. Magn. Reson. Med. 43(5), 682-690. https://doi.org/10.1002/(SICI)1522-
748 2594(200005)43:5<682::AID-MRM10>3.0.CO;2-G

749 Wang, Y., Liu, T., 2015. Quantitative susceptibility mapping (QSM): decoding MRI data for a
750 tissue magnetic biomarker. Magn. Reson. Med. 7, 82-101. https://doi.org/10.1002/mrm.25358

751 Weir, J. P., 2005. Quantifying test-retest reliability using the intraclass correlation coefficient
752 and the SEM. J. Strength Cond. Res. 19(1), 231-240.

753 Wharton, S., Bowtell, R., 2010. Whole-brain susceptibility mapping at high field: a comparison
754 of multiple-and single-orientation methods. Neuroimage 53(2), 515-525.
755 https://doi.org/10.1016/j.neuroimage.2010.06.070

756 Yacoub, E., Shmuel, A., Pfeuffer, J., Van de Moortele, P.F., Adriany, G., Andersen, P., Vaughan,
757 J.T., Merkle, H., Ugurbil, K., Hu, X., 2001. Imaging brain function in humans at 7 Tesla. Magn.
758 Reson. Med. 45, 588-594. https://doi.org/10.1002/mrm.1080

759 Yang, X., Sammet, S., Schmalbrock, P., Knopp, M. V., 2010. Postprocessing correction for
760 distortions in T2* decay caused by quadratic cross-slice b0 inhomogeneity. Magn. Reson. Med.
761 63(1): 1258-1268. https://doi.org/10.1002/mrm.22316

762 Yao, B., Li, T., van Gelderen, P., Shmueli, K., De Zwart, J.A., Duyn, J.H., 2009. Neuro image
763 susceptibility contrast in high field MRI of human brain as a function of tissue iron content.
764 Neuroimage 44(4), 1259-66. https://doi.org/10.1016/j.neuroimage.2008.10.029

765 Yao, B., van Gelderen, P., de Zwart, J.A., Duyn, J.H., 2007. Brain iron in MR imaging: R2* and
766 phase shift at different field strengths. Proc. Intr. Soc. Mag. Reson. Med. 15, 2165.

767 Zhou, D., Liu, T., Spincemaille, P., Wang, Y., 2014. Background field removal by solving the
768 Laplacian boundary value problem. NMR Biomed. 27(3), 312-319.
769 https://doi.org/10.1002/nbm.3064